Title

PROPERTIES OF THE SCUBA-2 850 mu m SOURCES IN THE AKARI NEP-DEEP FIELD

Permalink

https://escholarship.org/uc/item/6ff053nq

Journal

JOURNAL OF THE KOREAN ASTRONOMICAL SOCIETY, 51(3)

ISSN

1225-4614

Authors

Seo, Hyunjong
Jeong, Woong-Seob
Kim, Minjin
et al.

Publication Date

2018

DOI

10.5303/JKAS.2018.51.3.49

Peer reviewed

Properties of the SCUBA-2 850 μm Sources in the *AKARI* NEP-Deep Field

Hyunjong Seo[1], Woong-Seob Jeong[1,2], Minjin Kim[1,2], Seong Jin Kim[1,12], Jongwan Ko[1,2],
Jeonghyun Pyo[1], Min Gyu Kim[3,4], Chris Pearson[5,6,7], Laia Barrufet[5,6],
Maria del Carmen Campos Varillas[5], Hideo Matsuhara[8], Matt Malkan[9], Helen K. Kim[9],
Toshinobu Takagi[8], Takamitsu Miyaji[10,11], Jorge Díaz Tello[10,11], Tomotsugu Goto[12], and
Nagisa Oi[13]

[1]Korea Astronomy and Space Science Institute, 776 Daedukdae-ro, Yuseong-gu, Daejeon 34055, Korea; hjseo@kasi.re.kr
[2]Korea University of Science and Technology, 217 Gajeong-ro, Yuseong-gu, Daejeon 34113, Korea
[3]Genesia Corporation, Mitaka, Tokyo 181-0013, Japan
[4]Department of Physics and Astronomy, Seoul National University, Gwanak-gu, Seoul 08826, Korea
[5]RAL Space, Rutherford Appleton Laboratory, Chilton, Didcot, Oxfordshire OX11 0QX, UK
[6]School of Physical Sciences, The Open University, Milton Keynes, MK7 6AA, UK
[7]Oxford Astrophysics, Denys Wilkinson Building, University of Oxford, Keble Rd, Oxford OX1 3RH, UK
[8]Institute of Space and Astronautical Science, Japan Aerospace Exploration Agency, 3-1-1 Yoshinodai, Chuo-ku,
Sagamihara 252-5210, Japan
[9]Department of Physics and Astronomy, University of California, Los Angeles, CA 90024, USA
[10]Instituto de Astronomía sede Ensenada, Km 103 Carret. Tijuana-Ensenada, 22860, Ensenada, BC, Mexico
[11]PO BOX 439027, San Ysidro, CA 92143-9027, USA
[12]Institute of Astronomy, National Tsing Hua University, No. 101, Section 2, Kuang-Fu Road, Hsinchu, Taiwan
[13]Tokyo University of Science, 1-3 Kagurazaka, Shinjuku-ku, Tokyo 162-8601, Japan

Abstract: We carry out a study of Sub-Millimeter Galaxies (SMGs) in the *AKARI* NEP-Deep field using the James Clerk Maxwell Telescope (JCMT) SCUBA-2 850 μm source catalog, released as part of the SCUBA-2 Cosmology Legacy Survey (S2CLS) program. The SCUBA-2 850 μm map has a root mean square (rms) noise of 1.2 mJy beam^{-1} and covers an area of 0.60 degree^2. We find four SMGs which have counterparts to *Herschel* sources with spectroscopic redshifts in the literature. In addition, three dust obscured galaxies (DOGs) detected in *Herschel* bands are selected as a comparison sample. We derive IR luminosities of SMGs using the CIGALE code, which are similar to those of high redshift SMGs from previous studies. The contribution of AGN to the total IR luminosity in SMGs (2%–11%) is smaller than the lower limit for the one in DOGs (19%–35%), which is consistent with the expectation from the evolutionary scenario of massive galaxies. We search for SMGs in overdense regions as protocluster candidates and investigate four regions, including candidates around three DOGs. Finally, we argue that follow-up spectroscopic observation for the NEP-Deep field will provide crucial information to understand the role of SMGs in the evolution of massive galaxies.

Key words: galaxies: evolution — submillimeter: galaxies

1. Introduction

Recent studies of the IR luminosity density (or star formation rate density) show that it increases rapidly from the local Universe to $z \sim 1$ and flattens at around $z \sim 2$ (Gruppioni et al. 2013; Magnelli et al. 2013; Goto et al. 2015). Because re-radiated emission of starlight by dust is an important tracer of star formation, submillimeter galaxies (SMGs) at high redshift are one of the proper populations for understanding cosmic star formation history. According to the evolutionary scenario of massive galaxies in Dey et al. (2008, 2009), SMGs at high redshift are in a starburst phase as the early stage of major merging, and they evolve into dust obscured galaxies (DOGs) with increasing contribution by active galactic nuclei (AGN). Narayanan et al. (2010)

also suggest that SMGs represent the starburst phase in the earlier stage of the evolution of merger-driven bright DOGs. In terms of such evolutionary scenarios, a study of the link between SMGs and DOGs is important to understand the evolution of massive galaxies. For example, according to the standard evolutionary scenario, the contribution of AGN to the total IR luminosity in SMGs is expected to be smaller than that in DOGs. Although many SMGs are known to contain an AGN (Pope et al. 2008), the contribution of AGN to the bolometric luminosity is not significant (Pope et al. 2008; Menéndez-Delmestre et al. 2009) compared to DOGs in the literature (Riguccini et al. 2015; Toba et al. 2017b). However, the origin of DOGs and their relation to SMGs is still under debate. Several studies have argued that DOGs do not represent a unique
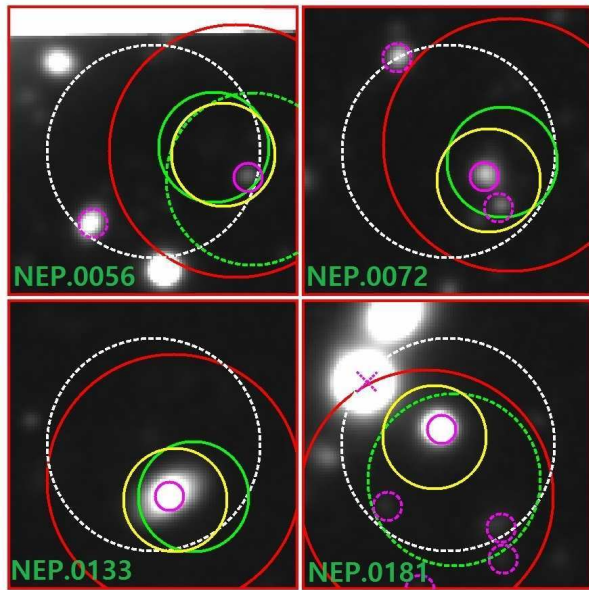
Figure 1. Post stamp images of four SMGs from Subaru/S-cam (Miyazaki et al. 2002) R_C band. The size of each stamp is $20'' \times 20''$. White, red, green (solid and dotted) and yellow circles represent FWHM of PSFs of SCUBA-2 850 μm, *Herschel*/SPIRE, *Herschel*/PACS (100 μm and 160 μm) and $AKARI$ mid-IR (L24) bands, which correspond to a diameter of $14''.8$, $17''.6$, $7''.7$, $12''.0$ and $7''.2$, respectively. All optical objects (Oi et al. 2014) located within the beam size of 850 μm and SPIRE bands are identified with magenta symbols. The magenta solid line circle represents the optical counterpart identified by LR analysis based on mid-IR band data. The magenta '×' represents an optical object that can be classified as a star candidate with the criteria of both stellarity (>0.95) and $u^*g'JKs$ color selection in Oi et al. (2014). The ID of each SMG comes from the 850 μm source catalog of Geach et al. (2017). North is up, east is left.

stage of galaxy evolution but are actually diverse populations of disk galaxies or gas-rich merging galaxies (Narayanan et al. 2010; Hwang et al. 2013). Moreover, there have been claims that the large flux density ratio between mid-IR and UV bands of DOGs is mainly due to abnormal faintness in the UV band rather than brightness in the mid-IR band due to the extra contribution of AGN (Penner et al. 2012; Hwang et al. 2013; Lee et al. 2016). Studies of the clustering of SMGs and DOGs also support a diversity of DOGs. Brodwin et al. (2008) report that the clustering correlation length of IR-faint DOGs ($S_\nu(24\mu m) < 0.5$ mJy) is similar to that of SMGs, which implies an evolutionary connection between the two populations. They additionally show that the clustering correlation length of DOGs increases for the brighter mid-IR DOGs. Toba et al. (2017a) also obtain a mid-IR flux dependence of the clustering using IR-bright DOGs (3.0 mJy $< S_\nu(22\mu m) < 5.0$ mJy). On the other hand, they show that the clustering strength of IR-bright DOGs is larger than that of SMGs (Hickox et al. 2012; Wilkinson et al. 2017) or IR-faint DOGs (Brodwin et al. 2008). Therefore, a comparison
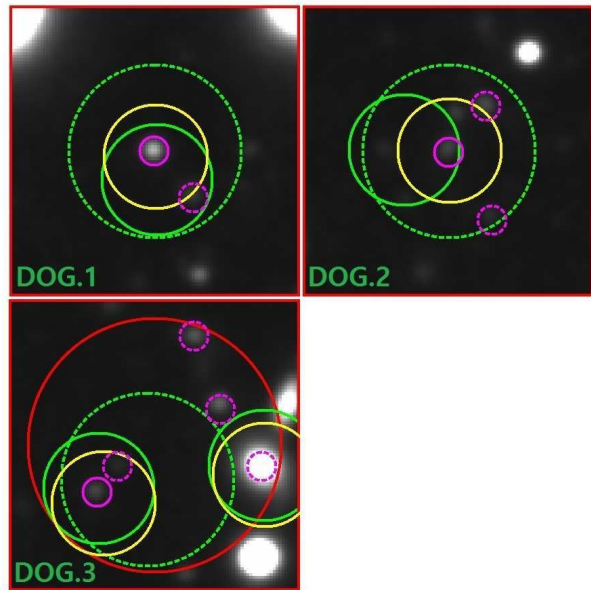
Figure 2. Post stamp images of three DOGs from Subaru/S-cam R_C band. The size of each stamp is $20'' \times 20''$. Symbols have the same meaning as in Figure 1. All optical objects (Oi et al. 2014) located within the beam size of PACS and SPIRE bands are identified with magenta symbols. The magenta solid line circle represents the DOG as well as the optical counterpart identified by LR analysis based on the mid-IR band. North is up, east is left.

of SMGs and DOGs is important, not only to understand the evolutionary sequence of massive galaxies but also to investigate the physical connection between the two populations.

Protoclusters at $z > 2$ are efficient sites for the study of high redshift galaxy populations and their evolution, because they are thought to be ancestors of present-day galaxy clusters (Venemans et al. 2002; Ouchi et al. 2004; Overzier et al. 2006). The typical diameter of a protocluster is diverse, ranging from 2 Mpc to 5 Mpc (Miley et al. 2004; Intema et al. 2006; Venemans et al. 2007). One popular method of searching for protoclusters is to measure the spatial number density of galaxies with similar redshift range. Because the mean redshift of SMGs is larger than two (Chapman et al. 2005; Wardlow et al. 2011; Casey et al. 2013), SMGs are a proper population for the study of protoclusters (Noble et al. 2013; Rigby et al. 2014; Casey et al. 2015; Clements et al. 2016). SMG overdensities around rare objects are also reported. For example, Jones et al. (2014, 2015) reported SMG overdensities around Hot DOGs (i.e., DOGs with blue mid-IR to far-IR color due to powerful AGN) and radio selected AGNs, which suggests that they (Hot DOGs and radio selected AGNs) could be possible signposts of protoclusters.

Therefore, SMGs are a useful population for the study of galaxy evolution. In this study, we use Submillimeter Common User Bolometer Array-2 (SCUBA-2; Holland et al. 2013) 850 μm sources in the $AKARI$

Table 1
IR and sub-millimeter photometric data for seven objects with spectroscopic redshift.

ID	$S_{2.4}$ (μJy)	$S_{3.2}$ (μJy)	$S_{4.1}$ (μJy)	S_7 (μJy)	S_9 (μJy)	S_{11} (μJy)	S_{15} (μJy)
NEP.0056	57.00±3.18	83.60±3.48	87.50±5.07	69.50±6.36	87.60±7.19	...	206.00±28.30
NEP.0072	32.80±2.69	49.00±2.63	51.90±3.06	40.40±6.04	43.10±7.34	67.80±12.30	156.00±18.00
NEP.0133	187.00±5.94	163.00±5.38	107.00±4.53	51.60±6.17	143.00±7.56	210.00±23.00	168.00±18.10
NEP.0181	...	...	...	530.00±10.30	631.00±21.40	684.00±41.10	1000.00±22.50
DOG.1	60.40±5.35	90.70±3.65	154.00±6.69	314.00±7.89	467.00±10.50	618.00±22.20	1050.00±22.60
DOG.2	35.50±2.75	56.00±2.78	61.50±3.31	55.90±6.22	87.40±9.40	124.00±26.60	442.00±20.00
DOG.3	60.70±3.25	116.00±4.18	194.00±7.03	382.00±16.20	519.00±9.15	601.00±19.50	797.00±45.70

S_{18} (μJy)	S_{24} (μJy)	S_{100} (mJy)	S_{160} (mJy)	S_{250} (mJy)	S_{350} (mJy)	S_{500} (mJy)	S_{850} (mJy)
326.00±20.60	558.00±53.90	7.34±1.37	25.19±4.42	36.54±3.46	44.05±2.85	30.78±3.62	5.13±1.38
316.00±20.50	462.00±108.00	12.59±1.83	...	44.36±8.63	42.08±6.64	24.40±8.94	5.25±1.44
214.00±30.00	292.00±51.20	2.86±2.44	...	22.55±3.44	19.40±2.66	11.80±3.36	4.12±1.35
1170.00±26.00	1460.00±85.50	...	30.70±10.54	49.99±3.91	50.27±3.15	28.25±4.19	3.89±1.31
1400.00±25.50	2070.00±181.00	12.58±3.33	10.85±4.39	...	...	...	...
431.00±56.00	848.00±136.00	8.02±2.81	9.35±3.08	...	...	...	...
953.00±91.20	1330.00±59.40	19.33±1.59	45.86±5.28	30.20±9.07	19.66±8.63	17.55±9.75	...

$S_{2.4} - S_{24}$: *AKARI*/IRC catalog (Murata et al. 2013).
$S_{100} - S_{500}$: *Herschel*/PACS & SPIRE catalogs (Pearson et al., in prep.). SPIRE fluxes are observed fluxes which are not corrected for flux boosting effect.
S_{850}: Deboosted flux density in Geach et al. (2017).

NEP-Deep field to study SMGs in terms of galaxy evolution. Due to continuous mid-IR coverage by *AKARI* observations, the NEP-Deep field (Matsuhara et al. 2006) is an efficient site for the study of galaxy evolution. We estimate the physical properties of SMGs by fitting spectral energy distributions (SEDs) of SMGs. The contribution of AGN in SMGs is compared with that in DOGs to investigate the link between them, and the evolution of massive galaxies. We search for SMG overdense regions in the NEP-Deep field and investigate several protocluster candidates. This paper is organized as follows. In Section 2, we present multi-wavelength observation data and samples of SMGs and DOGs. In Section 3, the matching of multi-wavelength catalogs and building SEDs of galaxies is described. In Section 4, galaxy SEDs are fitted using models. The results of this study are discussed in the final section. In this study, we assume a flat Universe with a set of cosmological parameters: $H_0 = 70$ km s^{-1} Mpc^{-1}, $\Omega_M = 0.3$ and $\Omega_\Lambda = 0.7$.

2. OBSERVATION DATA AND SAMPLES

2.1. Observation Data

The James Clerk Maxwell Telescope (JCMT) SCUBA-2 850 μm source catalog and mosaic map for the *AKARI* NEP-Deep field was released to the public as a part of SCUBA-2 Cosmology Legacy Survey (S2CLS) program (Geach et al. 2017). Among 3000 sources with 3.5σ detection in the S2CLS program, approximately 300 sources are located in the NEP-Deep field. PONG-2700 was used in observing mode for the NEP-Deep field, which covers an area of $45' \times 45'$ with a scan velocity of $600''$/sec in a single mapping procedure (Hol-
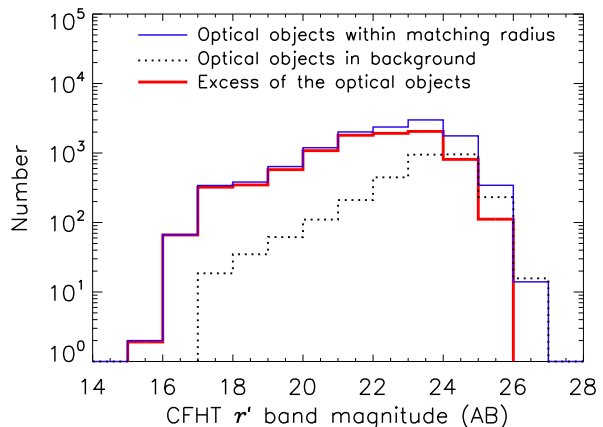
Figure 3. Various magnitude distributions of optical objects. The blue thin solid line is a distribution of objects within the matching radius around mid-IR objects, whereas the dotted line is a distribution of objects in the background. Subtraction of the two lines gives the red thick solid line, which results in $q(m)$ after the normalization in Equation (3).

land et al. 2013). The SCUBA-2 850 μm map has a root mean square (rms) noise of 1.2 mJy beam^{-1} and covers an area of 0.60 degree^2 centered at $(\alpha_{2000}, \delta_{2000}) = (17^h55^m53^s, +66°35'58'')$. The pixel scale of the map is $2''$ (refer to Geach et al. 2017 for more information about SCUBA-2 850 μm observation).

Counterparts of 850 μm sources in multi-wavelength bands were sought using various catalogs ranging from optical to sub-millimeter bands. Canada-France-Hawaii Telescope (CFHT)/MegaCam
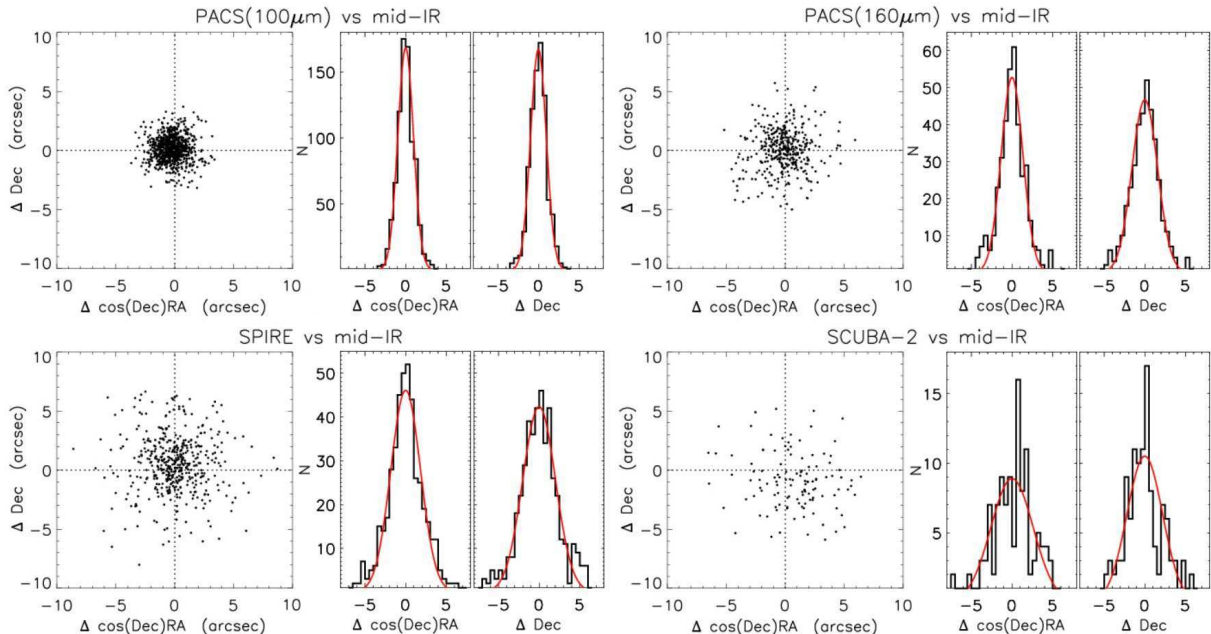
Figure 4. Positional uncertainty of far-IR or sub-millimeter band in comparison with mid-IR band. Dots represent relative positions of single matched mid-IR objects within the beam size of far-IR or sub-millimeter band. Mean offset and 1σ are presented in Table 2. Histograms are plotted after adjusting the mean offset and Gaussian-fitting is presented with red solid lines. Although the offset of SCUBA-2 shows some asymmetric distribution, other cases are well fitted with a Gaussian function.

Table 2
Positional uncertainty in comparison with mid-IR band.

Band	R.A. (arcsec) offset	σ	DEC (arcsec) offset	σ	Total σ
PACS 100μm	-0.2278	1.0446	0.1517	1.0488	1.4803
PACS 160μm	-0.1274	1.6911	0.0579	1.7645	2.4440
SPIRE	0.0028	2.3380	0.5224	2.4307	3.3726
SCUBA-2	0.7276	2.7610	-0.8834	2.3921	3.6531

Table 3
Counterpart identification at wavelengths beyond mid-IR.

ID	PACS 100μm	PACS 160μm	SPIRE	SCUBA-2
NEP.0056	○	○	○	△
NEP.0072	○	N	△	△
NEP.0133	○	N	○	○
NEP.0181	N	○	△	△
DOG.1	△	○	N	N
DOG.2	○	△	N	N
DOG.3	△	△	$-$	N

○: Single matching or the optical counterpart identified in the mid-IR band has the largest L with high reliability ($R > 0.8$) in that band. That is, the optical counterpart identified in the mid-IR band is still effective as the optical counterpart in that band.
△: The optical counterpart identified in the mid-IR band has the largest L with low reliability ($R < 0.8$) in that band. That is, although the optical counterpart identified in the mid-IR band is still the dominant contributor in that band, there is a possibility of contamination from other optical candidates.
N: No detection (i.e., the optical counterpart identified in mid-IR band is not detected in that band).
$-$: For the case of DOG.3, because the position of the SPIRE object is biased due to blending of two mid-IR (or two PACS) objects, LR analysis to identify the optical counterpart based on SPIRE band is inappropriate.

(u^*, g', r', i' and z' bands) covers optical bands with 4σ detection limits of 24.6 (5σ), 26.7, 25.9, 25.1 and 24.1 AB magnitude, respectively, and CFHT/WIRCam (Y, J and Ks bands) covers near-IR bands with 4σ detection limits of 23.4, 23.0 and 22.7 AB magnitude, respectively (Oi et al. 2014). $AKARI$/IRC (N2, N3, N4, S7, S9W, S11, L15, L18W and L24 bands) covers near- and mid-IR bands with 5σ detection limits of 11, 9, 10, 30, 34, 57, 87, 93 and 256 μJy, respectively (Murata et al. 2013). $Herschel$/PACS covers 100 and 160 μm with 3σ sensitivities of 4.8 and 9.6 mJy, respectively (Pearson et al., in prep.), in which source extraction is conducted for 100 and 160 μm separately. There is another PACS catalog whose photometry is conducted based on mid-IR prior positions, which was used to select 2 DOGs (i.e., DOG.1 and DOG.2). $Herschel$/SPIRE covers 250, 350 and 500 μm whose 1σ sensitivities are 9.0, 7.5 and 10.8 mJy, respectively (Pearson et al., in prep.).

2.2. Samples

In this study, we analyzed two different samples in the NEP-Deep field. First, we selected four SMGs in the SCUBA-2 850 μm catalog (Geach et al. 2017), which
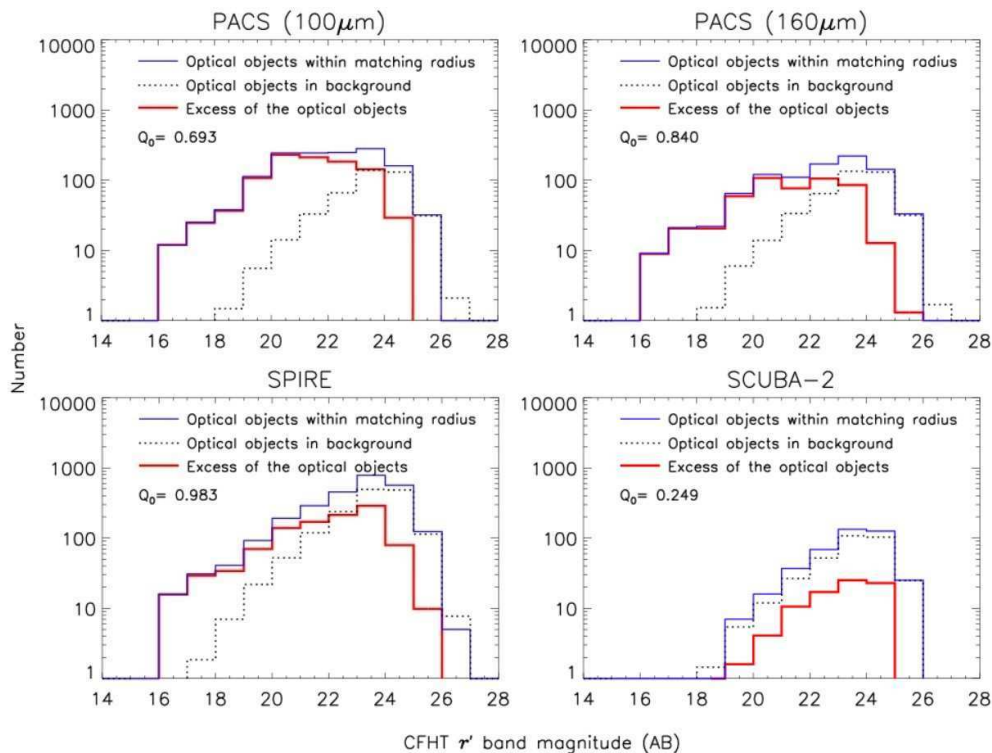
Figure 5. Various magnitude distributions of optical objects. The blue thin solid line is the distribution of optical objects within the matching radius of each band, whereas the dotted line is that of the background. Subtraction of the two lines yields the red thick solid line, which results in $q(m)$ after the normalization in equation (3).

were detected in the *Herschel*/PACS or SPIRE observations and have spectroscopic redshift information in the literature. These criteria were adopted to avoid false detection of SMGs and to obtain reliable results of SED fitting. Second, we identified three DOGs with spectroscopic redshift in the catalog of Murata et al. (2013) using the flux density ratio of *AKARI* L24 band to CFHT r' band with $S_\nu(\mathrm{L24})/S_\nu(r') \geq 982$ by following the criterion $S_\nu(24\mu m)/S_\nu(R) \geq 982$ used in Dey et al. (2008). These three DOGs are not detected in 850 μm observation but detected in *Herschel* observations. We used them as a comparison sample to investigate the evolution of massive galaxies. IR and sub-millimeter photometric data for the seven objects are presented in Table 1.

3. ANALYSIS OF COUNTERPARTS

To identify optical counterparts in multi-wavelength bands, we searched *AKARI* mid-IR objects within the beam size of 850 μm (Figure 1 for SMGs) and within the beam size of *Herschel* bands (Figure 2 for DOGs). First, we searched for an optical counterpart based on the *AKARI* mid-IR band. As shown in Figure 1, NEP.0072 has multiple optical candidates. To identify a reliable optical counterpart among multiple candidates, we conducted a likelihood ratio analysis (LR analysis; Sutherland & Saunders 1992; Smith et al. 2011; Kim et al. 2012; Seo et al. 2017) which considers the mag-

nitude of an optical object as well as positional offset. LR analysis was applied to *AKARI* mid-IR objects and the optical (CFHT r' band) objects. We estimated a parameter L for multiple optical candidates within the beam size of mid-IR object. Following Sutherland & Saunders (1992), the parameter L consists of two parts: A magnitude part and a position part as expressed below

$$L = \frac{q(m)f(r)}{n(m)}. \tag{1}$$

The magnitude part consists of $n(m)$ and $q(m)$ which are normalized magnitude distributions of optical objects for background and true counterpart of mid-IR object, respectively, while the position part $f(r)$ represents the probability distribution for the radial offset of the optical object from the mid-IR object. $f(r)$ is expressed using a Gaussian function as presented below

$$f(r) = \frac{1}{2\pi\sigma^2} \exp\left(\frac{-r^2}{2\sigma^2}\right), \tag{2}$$

where r and σ represent a distance and a positional uncertainty between mid-IR object and optical object, respectively. A σ value of $1''.556$, the positional accuracy between *AKARI* L24 band and CFHT z' band (Murata et al. 2013), was used as a representative positional uncertainty between mid-IR band and optical band. Mean offset between mid-IR object and optical object (Murata et al. 2013) was also considered in
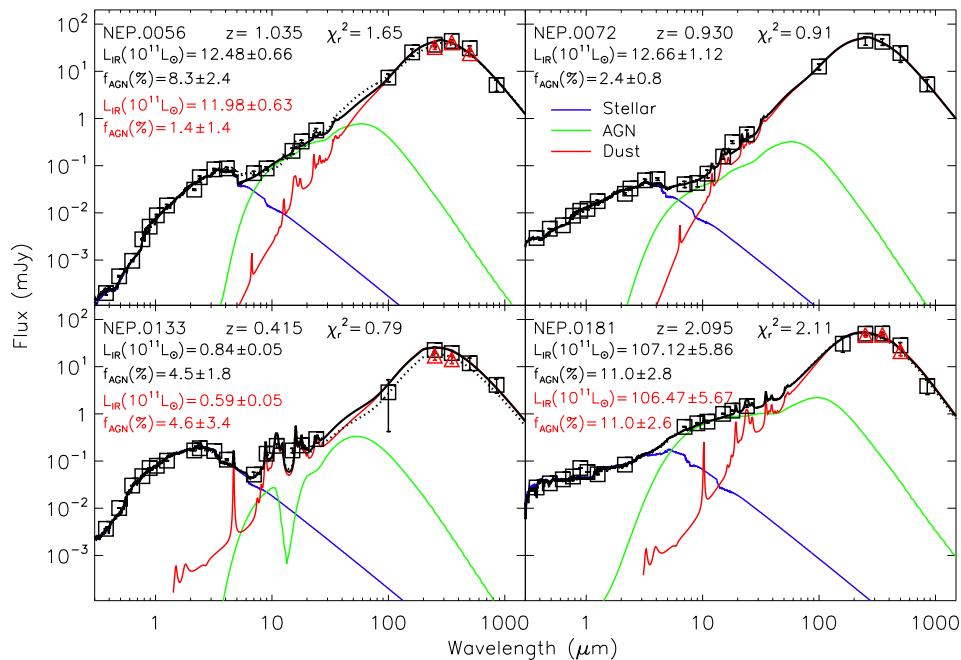
Figure 6. SEDs of four SMGs fitted with the CIGALE code. Black squares represent photometric data. Black solid lines represent the best-fit models which consist of three components: stellar (blue), AGN (green) and dust (red). L_{IR} represents total IR luminosity. The contribution of AGN, f_{AGN}, is defined as the ratio of AGN luminosity to the total IR luminosity (i.e., $= L_{IR}^{AGN}/L_{IR}$). Luminosities are estimated in the rest frame wavelength $8-1000$ μm. Red triangles are the deboosted SPIRE fluxes, and black dotted lines represent the best-fit models estimated by adopting the deboosted SPIRE fluxes instead of the observed SPIRE fluxes. The corresponding L_{IR} and f_{AGN} are presented in red font. Because the observed SPIRE flux at 500 μm of NEP.0133 cannot be corrected by the result of Wang et al. (2014) due to faintness, the black dotted line of NEP.0133 was estimated without the 500 μm flux. As NEP.0072 is located in the shallow SPIRE area, the test for deboosting by the result of Wang et al. (2014) is not appropriate (refer to Section 4).

the estimation of $f(r)$. To estimate $q(m)$, we found the magnitude distribution of optical objects within the matching radius (4″03, half the sum of FWHM of PSFs at $AKARI$ L24 band and CFHT z' band) around mid-IR objects. To estimate the magnitude distribution of optical objects in the background separately, we considered areas of equal size with $q(m)$ that are more than 4″03 away from mid-IR objects. A subtraction of two magnitude distributions was then conducted (red thick solid line in Figure 3). The result represents the excess magnitude distribution above the background of optical objects, and normalization of the result becomes $q(m)$ as presented below

$$q(m) = \frac{excess(m)}{\Sigma_m \ excess(m)} \ \times \ Q_0, \qquad (3)$$

where Q_0 is the fraction of counterparts and is estimated as follows

$$Q_0 = \frac{N_{candidates} - N_{background}}{N_{mid-IR}}, \qquad (4)$$

where $N_{candidates}$ and $N_{background}$ are the number of optical objects in the matching radius around mid-IR objects and in the background, respectively, and N_{mid-IR}

is the number of mid-IR objects. The value of Q_0 is calculated to be 0.844. The reliability R_j of the optical counterpart was estimated to confirm the validity of the identified counterpart compared with other candidates within the beam size of a given mid-IR object by following the expression in Sutherland & Saunders (1992):

$$R_j = \frac{L_j}{\Sigma_i \ L_i + (1 - Q_0)}, \qquad (5)$$

where subscript i represents each optical candidate within the beam size of a mid-IR object. The reliability of the optical counterpart for NEP.0072 is 0.828. The result is larger than 0.8, which indicates that the probability of false association is less than 20%. In this study, an optical candidate with $R \geq 0.8$ was considered as a robust counterpart. The same procedure was repeated for multiple optical candidates of DOG.3 (Figure 2). The reliability of the optical counterpart of DOG.3 is 0.821.

To confirm whether the optical counterpart identified in the mid-IR band is still effective as the optical counterpart at longer wavelength than mid-IR, we further conducted LR analysis based on PACS (100 μm and 160 μm), SPIRE and 850 μm bands. All optical objects (Oi et al. 2014) located within the beam
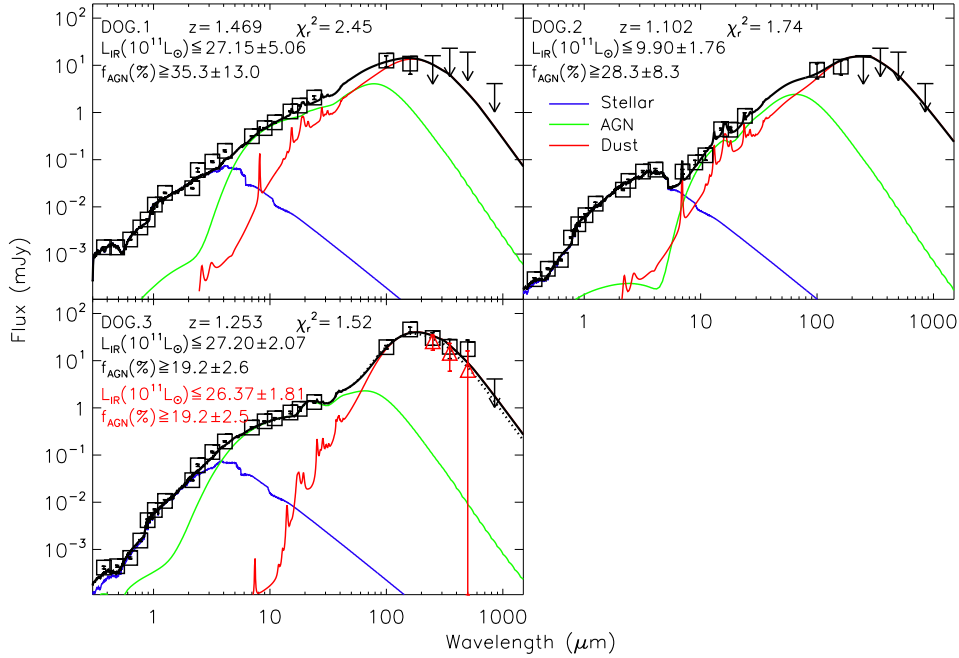
Figure 7. SEDs of three DOGs fitted with the CIGALE code. Black squares represent photometric data, which are used for SED fitting. Black solid lines represent the best-fit models which consist of three components: stellar (blue), AGN (green) and dust (red). The vertical arrows represent 50% completeness limits for SPIRE bands (Pearson et al., in prep.) and 850 μm (Geach et al. 2017), which are not used as input photometric data in the SED fitting procedure but presented to show that the fitted SED does not exceed the 50% completeness limits. Because there are no photometric data at longer wavelength bands than 160 μm (DOG.1 and DOG.2) or 500 μm (DOG.3), we constrain the fitted SED not to exceed the 50% completeness limits. Because the best-fit SED of DOG.2 exceeds the 50% completeness limits at SPIRE bands and 850 μm, we chose the model with the lowest χ^2 among those fitted that does not exceed the 50% completeness limits. On the other hand, the best-fit SEDs of DOG.1 and DOG.3 automatically satisfy the 50% completeness limits. The meaning of other symbols are same with those in Figure 6.

size of each band were considered as possible optical candidates. The difference with LR analysis based on mid-IR band is that we do not consider optical objects that can be classified as star candidates with the criteria of both stellarity ($>$0.95) and $u^*g'JKs$ color selection in Oi et al. (2014) because stars are unlikely to be detected at longer wavelength than the mid-IR band. Positional uncertainty in the far-IR or sub-millimeter bands compared to the optical band was estimated indirectly through the mid-IR band. First, a relative position to the mid-IR band was estimated for each band using a single matched mid-IR object within the beam size of each band (Figure 4 and Table 2). Then, the positional uncertainty between the optical band and far-IR or sub-millimeter band results in a quadratic sum of the value in Table 2 and the value of σ used in equation (2). The magnitude distributions of optical objects related with far-IR and sub-millimeter bands are presented in Figure 5.

The result of LR analysis is presented with various symbols in Table 3. The symbol '∘' indicates that the optical counterpart identified in the mid-IR band is still effective as the optical counterpart in that band, while the symbol '△' means that the optical counter-

part identified in the mid-IR band is still the dominant contributor in that band but there is a possibility of contamination from other optical candidates based on low reliability ($R <$0.8). We divided our targets into two groups based on the result in the PACS band. First, if the optical counterpart in the PACS band is robust (i.e., '∘' symbol of PACS band in NEP.0056, NEP.0072, NEP.0133 and NEP.0181), we conclude that the object has a single robust optical counterpart. Second, if the optical counterpart in the PACS band is less robust (i.e., '△' symbol of PACS band in DOG.1, DOG.2 and DOG.3), we conclude that the optical counterpart of the object is less robust at longer wavelength than mid-IR. For these sources, the photometric data of PACS and SPIRE are treated as upper limits in those bands.

4. SED

For the case of DOG.3, as shown in Figure 2, the beam area of the SPIRE band contains two mid-IR (or two PACS) objects. Because the position of SPIRE object is biased due to blending of two mid-IR objects, LR analysis to identify an optical counterpart based on SPIRE band is inappropriate. Since the two mid-IR objects share one SPIRE source, we divided their contributions
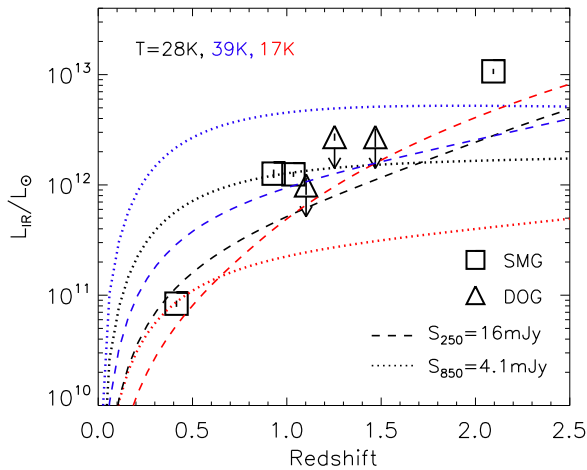
Figure 8. Total IR luminosities of galaxies as a function of redshift. Squares represent four SMGs, and triangles represent three DOGs. Most objects at $z > 0.9$ are ultraluminous infrared galaxies (ULIRGs). The luminosity limits of 250 μm (dashed line) and 850 μm (dotted line) are estimated using a single temperature modified blackbody (MBB) function with an optically thin assumption, $S_\nu = \nu^\beta B_\nu(T)$, where the Wien side of the MBB function is replaced by a power-law SED, $S_\nu = \nu^{-\alpha}$. $B_\nu(T)$ is the Planck function, and the dust emissivity index and mid-IR power-law index are $\beta = 1.5$ and $\alpha = 2$, respectively (Casey et al. 2013). Because the luminosity limit of 850 μm is sensitive to the dust temperature (unlike 250 μm), those with three dust temperatures which correspond to the mean, maximum and minimum dust temperatures of four SMGs, respectively, are presented. To estimate dust temperatures of SMGs, flux densities at $\lambda \geq 100$ μm are fitted by the MBB function. Flux densities of 16 mJy and 4.1 mJy correspond to 50% completeness limits of 250 μm and 850 μm, respectively.

to the SPIRE band flux density. Because a separation between two mid-IR objects ($11''$) is smaller than the pixel size at 500 μm of SPIRE band, deblending with publicly available software is unsuccessful. Therefore, we deblended their contributions manually. We estimated a pixel value in the SPIRE map at the position of each mid-IR object by 2D interpolation after subtraction of the mean sky value. Because the pixel values are correlated with one another due to their close positions, we assumed a Gaussian function (FWHM = beam size at each SPIRE band) to estimate such contributions and subtracted them from the pixel values. The deblended flux density at the SPIRE band for each mid-IR object was then estimated by a Gaussian function having the pixel value as a peak.

In order to estimate IR luminosities of SMGs and DOGs in the NEP-Deep field, SEDs with prior redshift information were fitted using Code Investigating GALaxy Emission (CIGALE[1]) v0.11 (Burgarella et al. 2005; Noll et al. 2009; Boquien et al., in prep.; Burgarella et al., in prep.) which allows us to investigate the physical properties (dust luminosity, AGN luminos-

ity, stellar mass, dust mass, etc.) of galaxies with the photometric data ranging from UV to far-IR. CIGALE derives physical parameters using models by varying star formation history, stellar population, dust attenuation, dust emission and AGN emission. The best fitting parameters and their uncertainties are determined by the mean and standard deviation of the probability distribution function (PDF; Noll et al. 2009). We adopted the double decreasing exponential star formation history module (`sfh2exp`) in the code as a star formation history, which is adequate to fit the observed photometric data due to two kinds of stellar population; the oldest population and the younger starburst population. The model from Maraston (2005) was used for the stellar population. Because the Maraston (2005) model includes a contribution from the thermally pulsating asymptotic giant branch (TP-AGB) stars, it is superior to fit the photometric data of near-IR bright sources. We used the Calzetti et al. (2000) model for dust attenuation with extinction free parameter for the young population, $E(B - V)$. For dust emission, we tested both DL2014 (Draine et al. 2007) and Dale2014 (Dale et al. 2014) models, and choose the DL2014 model because it shows a better fitting result. Because most SMGs are known to contain AGN (Pope et al. 2008), we added an AGN model based on Fritz et al. (2006) for SED fitting, which consists of three components; emission from central source, scattered light by torus and thermal emission from torus. We considered most angles between the equatorial plane of the torus and line of sight, ψ, ranging $\psi = 0-90°$ with interval of 20°.

Results of SED fitting for SMGs and DOGs are presented in Figure 6, Figure 7 and Table 4. The SED fit yields total IR luminosity $L_{IR} \sim 1-107 \times 10^{11}$ $L_\odot$ for the SMGs (Figure 8). These values are similar to the properties of SMGs in the literature (Clements et al. 2008; Casey et al. 2013; da Cunha et al. 2015; Seo et al. 2017). Because the photometric data of PACS and SPIRE bands in DOG.1, DOG.2 and DOG.3 are treated as upper limits and used for the SED fitting, the total IR luminosities of the three DOGs should be treated as upper limits. Both SPIRE and 850 μm fluxes can be subject to a flux boosting effect due to the contribution of instrumental noise and undetected faint objects within their large beam size. In this study, as presented in Table 1, the deboosted flux is used in 850 μm, while the observed fluxes which are not corrected for flux boosting are used in SPIRE bands. Although we did not estimate an amount of flux boosting in SPIRE bands specifically by simulation, we tested the effect of flux boosting on the contribution of AGN using results taken from the literature. Among various *Herschel* fields in Wang et al. (2014), 5σ instrumental noise of SPIRE observation in ELAIS S1 SWIRE field (25.8, 21.2 and 30.8 mJy at 250, 350 and 500 μm, respectively) is similar with that of a deep KPGT[2] obser-

---

[1] http://cigale.lam.fr

[2] A deep *Herschel*/SPIRE $30' \times 30'$ observation centered at NGC 6543 as part of the Key Program Guaranteed Time (KPGT; obsID = 1342188590) covers the *AKARI* NEP-Deep field partially. The region outside the deep KPGT area is cov-
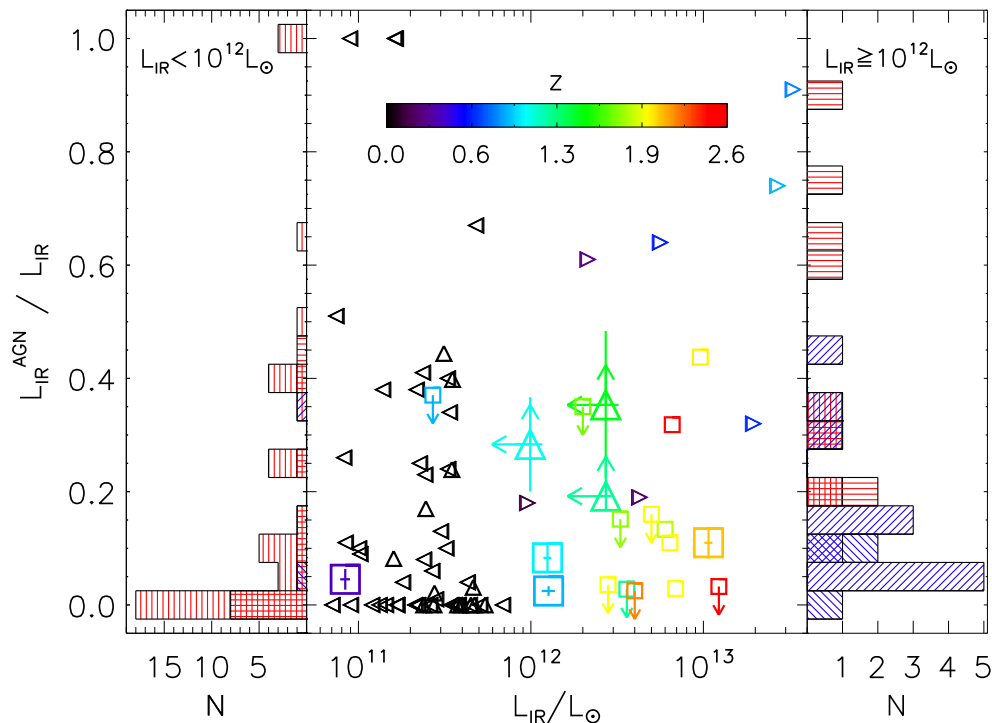
Figure 9. The contribution of AGN to the total IR luminosity versus the total IR luminosity. Squares and triangles represent SMGs and DOGs, respectively. Large and small symbols represent results in this study ($f_{AGN}1$ in Table 4) and those in the literature, respectively. Left-facing, small upward and right-facing triangles denote DOGs in Hwang et al. (2013), Lee et al. (2016) and Toba et al. (2017b), respectively, and small squares denote SMGs in Pope et al. (2008). Histograms with blue and red denote SMGs and DOGs, respectively. The left histograms are for objects with $L_{IR} < 10^{12} \ L_\odot$ (hatched with blue \\: SMG, hatched with blue //: Pope et al. 2008, hatched with red ||: Hwang et al. 2013, hatched with red =: Lee et al. 2016), whereas the right histograms are for sources with $L_{IR} \geq 10^{12} \ L_\odot$ (hatched with blue \\: SMG, hatched with blue //: Pope et al. 2008, hatched with red ||: DOG, hatched with red =: Toba et al. 2017b). Only far-IR detected objects in Hwang et al. (2013) are presented here. Error bars for sources taken from the literature are not plotted to avoid confusion.

vation in the NEP-Deep field (26.0, 21.5 and 31.0 mJy at 250, 350 and 500 μm, respectively). Therefore, a correction for flux boosting in SPIRE bands was tested using the result of the ELAIS S1 SWIRE field[3], and the contribution of AGN was estimated again by adopting the deboosted SPIRE fluxes in the SED fitting procedure. The deboosted SPIRE fluxes (red triangles) and the corresponding fitted SEDs (black dotted lines) are presented in Figure 6 and Figure 7, and the contribution of AGN ($f_{AGN}2$) is presented in Table 4 along with that corresponding to the observed SPIRE fluxes ($f_{AGN}1$). As shown, most f_{AGN} are almost unchanged after the correction for flux boosting in SPIRE bands.

---

5. Discussion and Summary

5.1. Contribution of AGN

According to the evolutionary scenario of massive galaxies, the DOG phase is preceded by a SMG in galaxy merger, which increases the contribution of AGN. Therefore, the contribution of AGN to the total IR luminosity in SMGs is expected to be smaller than that in DOGs. To test this evolutionary scenario, we estimated the contribution of AGN, f_{AGN}, for both four SMGs and three DOGs in the NEP-Deep field. f_{AGN} was estimated by a ratio of AGN luminosity to the total IR luminosity. As the upper limit of the total IR luminosity originates from upper limits of flux densities at longer wavelength bands than 100 μm, where the contribution of dust becomes significant compared to that of AGN, the upper limit of the total IR luminosity mainly corresponds to the upper limit of the dust luminosity. Therefore, the upper limit of the total IR luminosity of the DOGs translates into a lower limit of the contribution of AGN. As shown in Figure 9, the contribution of AGN in SMGs ranges from 2% to 11%, and we find no clear correlation between AGN contribution and the to-

Table 4
The contribution of AGN in SMGs and DOGs

ID	R.A.[a] (h:m:s)	DEC (d:m:s)	z^{b}	L_{IR} $(\times 10^{11} L_\odot)$	$f_{AGN}1^{\mathrm{c}}$ (%)	$f_{AGN}2^{\mathrm{c}}$ (%)	$A_{V,cont}^{\mathrm{d}}$ (mag)
NEP.0056	17:56:32.7	+66:33:20.9	1.035	12.48±0.66	8.3±2.4	1.4±1.4	2.3
NEP.0072	17:53:12.8	+66:41:12.1	0.930	12.66±1.12	2.4±0.8	...	1.4
NEP.0133	17:57:15.6	+66:44:06.0	0.415	0.84±0.05	4.5±1.8	4.6±3.4	0.8
NEP.0181	17:56:34.6	+66:27:17.6	2.095	107.12±5.86	11.0±2.8	11.0±2.6	0.6
DOG.1	17:56:04.0	+66:29:35.5	1.469	≤27.15±5.06	≥35.3±13.0	≥35.3±13.0	1.3
DOG.2	17:56:05.4	+66:33:29.5	1.102	≤9.90±1.76	≥28.3±8.3	≥28.3±8.3	2.0
DOG.3	17:56:22.0	+66:40:02.6	1.253	≤27.20±2.07	≥19.2±2.6	≥19.2±2.5	2.4

[a] (R.A., DEC) represents the position of the optical counterpart.
[b] Spectroscopic redshift data based on DEIMOS and GTC observations are not currently publicly available, and are used in this study with permission.
[c] $f_{AGN}1$ was estimated by adopting the observed SPIRE fluxes, while $f_{AGN}2$ was estimated by adopting the deboosted SPIRE fluxes (refer to Section 4). Because DOG.1 and DOG.2 are not detected in SPIRE bands, their $f_{AGN}1$ and $f_{AGN}2$ measurements are identical. The error of f_{AGN} is estimated by applying the error propagation formula (Bevington & Robinson 1992, page 43) on the definition of f_{AGN} and the errors of AGN luminosity and total IR luminosity.
[d] The fitted dust attenuation of the stellar continuum at the V band (5500 Å), which is estimated with the extinction curve in Calzetti et al. (2000). Although $A_{V,cont}$ of DOGs seems to be slightly larger than that of SMGs, they span a similar range. The result ($A_{V,cont}$=0.6−2.4) is similar with that of SMGs in the literature (Borys et al. 2005, the ensemble average of $A_{V,cont}$=1.7±0.3). It is also comparable with the visual extinction estimated from nebular emission lines for SMGs (Takata et al. 2006, $A_{V,neb}$∼1−4) or local DOGs (Hwang et al. 2013, $A_{V,neb}$∼0.8−4.7) when considering the calibration between two quantities, $A_{V,cont} = 0.44 A_{V,neb}$ (Calzetti et al. 2000; Wuyts et al. 2011). The $A_{V,neb}$ of Hwang et al. (2013) is estimated here by the observed flux ratio of Hα/Hβ ∼ 3.6−11 assuming the extinction curve in Calzetti et al. (2000) with the intrinsic flux ratio of Hα/Hβ = 2.86.
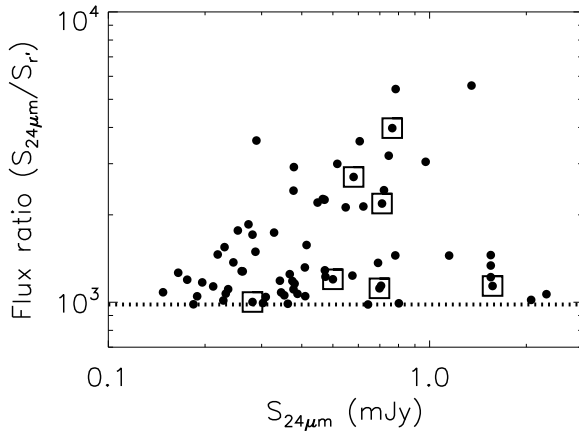

Figure 10. DOGs detected in 850 μm observation. Dots represent DOGs which are obtained from the *AKARI* catalog (Murata et al. 2013). Among them, seven DOGs (dots enclosed by squares) are detected in the 850 μm band, which are not part of the DOG sample in Figure 7 due to the absence of spectroscopic redshifts but discussed in Section 5.1 to support the conclusion of this study. Note that, in order to show robust cases for DOGs, only objects whose mid-IR detection is single matched with optical detection are presented here.

tal IR luminosity. This result is broadly consistent with previous studies which report that the contribution of AGN to the luminosity of SMGs is not significant even though many SMGs contain AGN. For example, Pope et al. (2008) reported that the AGN contribution to the mid-IR luminosity of SMGs is at most 30% and the total IR luminosity is dominated by star formation rather than AGN. Menéndez-Delmestre et al. (2009) reported

that the contribution from AGN to the bolometric luminosity of SMG is less than 32%. Although some studies reported a correlation between the AGN contribution and IR luminosity for some galaxy populations (LIRGs and ULIRGs: Lee et al. 2012; DOGs: Riguccini et al. 2015; Toba et al. 2017b), it is hard to recognize such correlation for SMGs in this study due to the small number of objects.

For the case of DOGs with $L_{IR} > 10^{12} L_\odot$ in the NEP-Deep field, although they give lower limits, the AGN contribution ranges from 19% to 35%, which is larger than that of SMGs. Other studies also show such large AGN contributions for DOGs with similar luminosity. Riguccini et al. (2015) reported that the AGN contribution of DOGs with $L_{8\mu m} > 2 \times 10^{12} L_\odot$ is larger than 20%. Toba et al. (2017b) reported that the AGN contribution ranges between 18%−91% for DOGs with $L_{IR} \geq 10^{12} L_\odot$. On the other hand, results for DOGs with $L_{IR} < 10^{12} L_\odot$ in the literature are more diverse (Figure 9). For local DOGs ($0.05 < z < 0.08$) in Hwang et al. (2013), 43% of their sources have a large AGN contribution ($f_{AGN} > 20\%$), while 57% of their sources show a small AGN contribution ($f_{AGN} < 20\%$). For local DOGs ($0.05 < z < 0.08$) in Lee et al. (2016), DOGs with power-law type show a large AGN contribution ($f_{AGN} > 20\%$), while DOGs with bump type have a small AGN contribution ($f_{AGN} < 20\%$). Therefore, for objects with $L_{IR} < 10^{12} L_\odot$, the distributions of AGN contribution between SMGs and DOGs does not appear to be distinctive. The AGN contribution in SMGs and DOGs with $L_{IR} > 10^{12} L_\odot$ in this study are consistent with the expectation from the evolutionary scenario of massive galaxies, which suggests that DOGs follow SMGs, with increasing contribution from AGN. On the other hand, for the objects with $L_{IR} < 10^{12} L_\odot$,
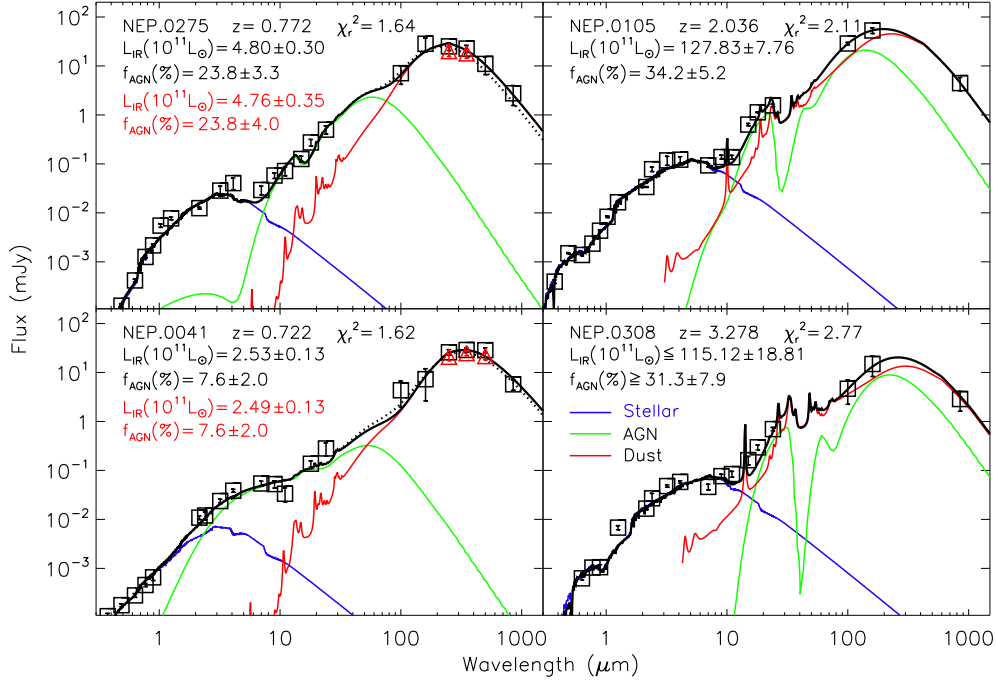
Figure 11. SEDs of four DOGs detected in 850 μm data. Redshifts are photometric redshifts given in Oi et al. (2014). The meaning of all symbols are the same as those in Figure 6 or Figure 7. Unlike the DOGs in Figure 7, we did not constrain the fitted SED by the 50% completeness limits of SPIRE bands because there are photometric data at 850 μm. Because the observed SPIRE flux at 500 μm of NEP.0275 cannot be corrected by the result of Wang et al. (2014) due to its faintness, the black dotted line of NEP.0275 was estimated without the 500 μm flux.

the result seems to be not consistent with the evolutionary scenario.

Besides the small number of objects, another caveat to this study is that SMGs and DOGs are not selected in a homogeneous manner: SMGs are selected from 850 μm data, while DOGs are selected from *Herschel* data. In order to overcome limitations due to the selection effect, it is required to conduct this study with sources selected in the same manner. For example, as shown in Figure 10, seven DOGs in the NEP-Deep field are detected in 850 μm observation. If we use these seven DOGs for this study instead of DOGs selected in *Herschel* data, we can compare the AGN contribution to SMGs and DOGs by reducing the selection effect. Although we plan to obtain spectroscopic redshifts for additional DOGs (e.g., the seven DOGs in Figure 10) by follow-up observation, the DOGs detected in 850 μm observation were treated in advance using photometric redshift to confirm the conclusion of this study. For such purpose, we considered photometric redshifts in Oi et al. (2014), and found that photometric redshift is more accurate, $\sigma_{\Delta z/(1+z)}=0.113$, when mid-IR detection is single matched with optical detection. Among the seven DOGs in Figure 10, four are considered in this study because they have photometric redshifts and satisfy the multi-wavelength matching criteria described in Section 3. Their SEDs are fitted with the CIGALE code and results are presented in Figure 11. As shown,

the AGN contributions are 8% and 24% at $L_{IR} < 10^{12}$ $L_\odot$, but 31% and 34% at $L_{IR} > 10^{12}$ $L_\odot$. For 850 μm selected DOGs with $L_{IR} > 10^{12}$ $L_\odot$, the AGN contribution is larger than that of SMGs in Figure 6 and consistent with that of *Herschel* selected DOGs in Figure 7. However, it should be noted that the range of redshift and luminosity is different among the samples. Although the result of 850 μm selected DOGs still seems to support the evolutionary scenario, we will estimate it again using more accurate spectroscopic redshifts in a follow-up study. Although we tried to reduce the selection effect using 850 μm selected DOGs, there still remains the possibility of a biased result due to another kind of selection effect. For example, as shown in Figure 12, the four SMGs are not the brightest objects both at 250 μm and 850 μm. They are selected because they have known spectroscopic redshifts, robust optical counterparts and are detected by *Herschel*. For this reason, SMGs with faint optical counterparts, SMGs with lower dust temperatures and high redshift SMGs are unlikely to be included in this study. To overcome such limitation due to this selection effect, it is required to conduct this study with a large number of sources. It may be a more efficient way to understand the evolution of massive galaxies. We are going to extend this study using a larger number of SMGs and DOGs by follow-up spectroscopic observation for the NEP-Deep field.
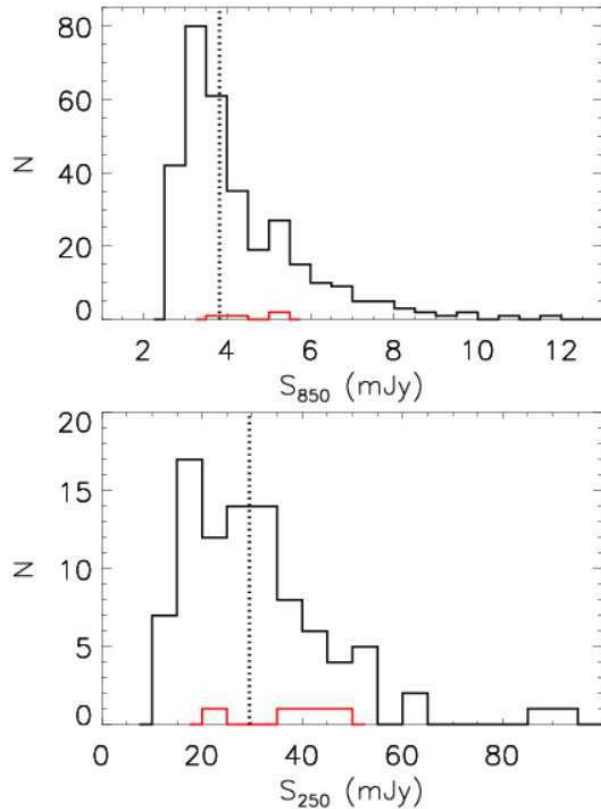
Figure 12. Top: 850 μm flux densities of all SMGs in the NEP-Deep field (Geach et al. 2017, black, dotted line: median) and the four SMGs in Figure 6 (red). Bottom: 250 μm flux densities of SPIRE objects that are located within the beam size of all SMGs (black, dotted line: median) and the four SMGs in Figure 6 (red).
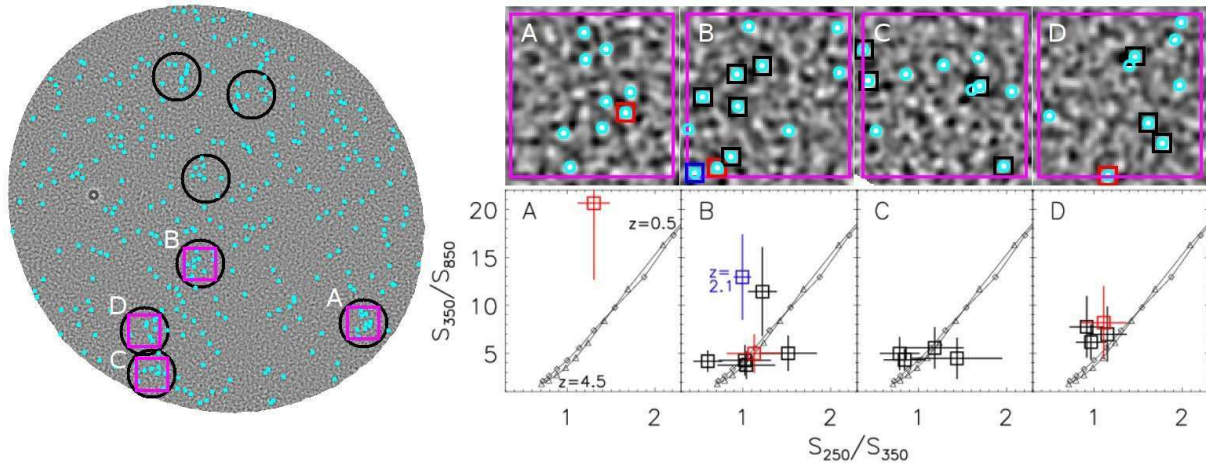
5.2. Protocluster Candidates

Because the mean redshift of SMGs is larger than two (Chapman et al. 2005; Wardlow et al. 2011; Casey et al. 2013), SMGs are often used to search for protoclusters. Therefore, we examined protocluster candidates by searching for SMG overdense regions within the area of $4' \times 4'$ which corresponds to 2 Mpc $\times$ 2 Mpc at $z = 2$. The size of 2 Mpc represents the smallest size of a protocluster in the literature (Miley et al. 2004; Intema et al. 2006; Venemans et al. 2007). Searching for SMG overdense regions is the first step to find a protocluster. To identify a SMG overdense region, we conducted a simulation using a simulated catalog which consists of uniformly distributed objects with the same number of sources in the observed 850 μm catalog. We then positioned a square with the FOV of $4' \times 4'$ randomly 5000 times and counted the number of simulated objects within the square each time. Such a simulation was iterated 100 times using 100 simulated catalogs. We then applied the same procedure to the observed 850 μm catalog (Geach et al. 2017) and found that on average 2.47 SMGs are counted within the square and the maximum number of SMGs within the square is 12.
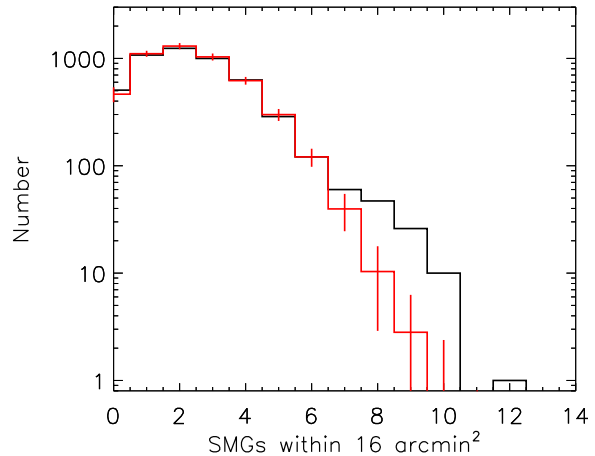
Figure 13. Histograms for number count of SMGs within a confined area. Black histogram represents the number of observed SMGs within an area of $4' \times 4'$ by positioning the area of $4' \times 4'$ randomly 5000 times. The same procedure was performed for uniformly distributed simulated SMGs (red histogram). The simulation was iterated 100 times using 100 simulated catalogs. Error bars represent the standard deviation of 100 iterations.

As shown in the results of the simulation (Figure 13), up to seven SMGs within the square can be treated as a result of random distribution, whereas more than eight SMGs within the square can be a sign of a clustering event due to the existence of a protocluster or large scale structure. For this reason, to find a SMG overdense region, we focused only on the region where more than eight SMGs are counted within the square. Therefore, by scanning the NEP-Deep field with the square in steps of $30''$ toward (R.A., Dec.) directions, we searched for SMG overdense regions where more than eight SMGs are counted within the square. As a result, we found seven SMG overdense regions in the NEP-Deep field, which are denoted by large circles in Figure 14.

Among these overdense regions, we focused on four regions as possible protocluster candidates and prioritized them for the follow-up study. We choose three of the regions as protocluster candidates because at least three SMGs seem to lie at similar redshift range judging from similar $Herschel$ and SCUBA-2 colors (regions denoted by B, C and D in Figure 14). Protocluster candidates in the region of B, C and D seem to lie at redshift $z = 2-3$ judging from the redshift tracks of Arp220 and M82. Second, we selected the region denoted by A also as a possible protocluster candidate. Jones et al. (2014) reported unusual SMG overdensity around Hot DOGs, which suggests that Hot DOGs could be a possible signpost of protoclusters. It follows that a SMG overdense region around rare objects, such as DOGs, can be a possible protocluster candidate. As discussed earlier, seven DOGs in the NEP-Deep field are detected in the 850 μm band. Among them, three DOGs are located in SMG overdense regions denoted by A, B and D in Figure 14. Therefore, the region A is one of the strongest candi-

Figure 14. Protocluster candidates. Left: SCUBA-2 850 μm image of the NEP-Deep field (Geach et al. 2017). Open cyan circles are SCUBA-2 850 μm sources. Black circles represent SMG overdense regions. Among them, 4 interesting regions are denoted by magenta squares. A FOV of the magenta square is $4' \times 4'$ which corresponds to 2 Mpc × 2 Mpc at $z = 2$. Right: SCUBA-2 and *Herschel* colors of 850 μm sources. Squares are 850 μm sources detected in *Herschel* bands. A blue square represents 850 μm source with spectroscopic redshift, and red squares are 850 μm sources classified as DOGs. Black solid lines and symbols are the redshift tracks of Arp220 (triangles) and M82 (diamonds) ranging $z = 0.5-4.5$ with the interval of $\Delta z = 0.5$.

dates because there are eight SMGs around a DOG. Although most SMGs in this region are not detected in *Herschel* bands, they do not seem to be false detections because they are detected at a significance of $>3.8\sigma$ in 850 μm observations, which indicates that the false detection rate for each SMG in region A is less than 10% (Geach et al. 2017). The protocluster candidate in region A seems to lie at redshift $z > 3$ because source extraction of *Herschel*/SPIRE data was conducted from the 250 μm map. The regions A, B, C and D are overdense by factors of 3.6, 4.9, 4.0 and 3.6 compared to the average SMG number density in the NEP-Deep field. A follow-up spectroscopic observation can confirm the protocluster candidates in this study.

Although the results of this study are restricted due to the small number of sources, we show the availability of SMGs as a proper population for the study of galaxy evolution. As a successive study, we plan follow-up spectroscopic observation for the NEP-Deep field with MMT/Hectospec, which will provide the spectroscopic redshift of about 60 optical counterparts with $r' < 23.5$ AB magnitude by four hours of exposure time. Along with the results in this study, further observational data will be useful for the discussion regarding SMGs in terms of the evolution of massive galaxies.

REFERENCES

Bevington, P. R., & Robinson, D. K. 1992, Data Reduction and Error Analysis for the Physical Sciences, 2nd edn. (New York: McGraw-Hill)

Borys, C., Smail, I., Chapman, S. C., et al. 2005, The Relationship between Stellar and Black Hole Mass in Submillimeter Galaxies, ApJ, 635, 853

Brodwin, M., Dey, A., Brown, M. J. I., et al. 2008, Clustering of Dust-Obscured Galaxies at $z \sim 2$, ApJ, 687, 65

Burgarella, D., Buat, V., & Iglesias-Páramo, J. 2005, Star Formation and Dust Attenuation Properties in Galaxies from a Statistical Ultraviolet-To-Far-Infrared Analysis, MNRAS, 360, 1413

Calzetti, D., Armus, L., Bohlin, R. C., et al. 2000, The Dust Content and Opacity of Actively Star-Forming Galaxies, ApJ, 533, 682

Casey, C. M., Chen, C.-C., Cowie, L. L., et al. 2013, Characterization of SCUBA-2 450 μm and 850 μm Selected Galaxies in the COSMOS Field, MNRAS, 436, 1919

Casey, C. M., Cooray, A., Capak, P., et al. 2015, A Massive, Distant Proto-Cluster at $z = 2.47$ Caught in a Phase of Rapid Formation?, ApJL, 808, 33

Chapman, S. C., Blain, A. W., Smail, I., et al. 2005, A Redshift Survey of the Submillimeter Galaxy Population, ApJ, 622, 772

Clements, D. L., Braglia, F., Petitpas, G., et al. 2016, H-ATLAS: A Candidate High Redshift Cluster/Protocluster of Star-Forming Galaxies, MNRAS, 461, 1719

Clements, D. L., Vaccari, M., Babbedge, T., et al. 2008, The SCUBA Half-Degree Extragalactic Survey (SHADES) – VIII. The Nature of Faint Submillimetre Galaxies in SHADES, SWIRE and SXDF Surveys, MNRAS, 387, 247

da Cunha, E., Walter, F., Smail, I. R., et al. 2015, An ALMA Survey of Sub-Millimeter Galaxies in the Extended Chandra Deep Field South: Physical Properties Derived from Ultraviolet-To-Radio Modeling, ApJ, 806, 110

Dale, D. A., Helou, G., Magdis, G. E., et al. 2014, A Two-Parameter Model for the Infrared/Submillimeter/Radio Spectral Energy Distributions of Galaxies and Active Galactic Nuclei, ApJ, 784, 83

Dey, A., Soifer, B. T., Desai, V., et al. 2008, A Significant Population of Very Luminous Dust-Obscured Galaxies at Redshift $z \sim 2$, ApJ, 677, 943

Dey, A., & Ndwfs/MIPS Collaboration 2009, The Pedigrees of DOGs (Dust-Obscured Galaxies), ASPC, 408, 411

Draine, B. T., & Li, A. 2007, Infrared Emission from Interstellar Dust. IV. The Silicate-Graphite-PAH Model in the Post-Spitzer Era, ApJ, 657, 810

Fritz, J., Franceschini, A., & Hatziminaoglou, E. 2006, Revisiting the Infrared Spectra of Active Galactic Nuclei with a New Torus Emission Model, MNRAS, 366, 767

Geach, J. E., Dunlop, J. S., Halpern, M., et al. 2017, The SCUBA-2 Cosmology Legacy Survey: 850 μm Maps, Catalogues and Number Counts, MNRAS, 465, 1789

Goto, T., Oi, N., Ohyama, Y., et al. 2015, Evolution of Mid-Infrared Galaxy Luminosity Functions from the Entire AKARI NEP Deep Field with New CFHT Photometry, MNRAS, 452, 1684

Gruppioni, C., Pozzi, F., Rodighiero, G., et al. 2013, The Herschel PEP/HerMES luminosity function – I. Probing the evolution of PACS selected Galaxies to z = 4, MNRAS, 432, 23

Holland, W. S., Bintley, D., Chapin, E. L., et al. 2013, SCUBA-2: the 10 000 Pixel Bolometer Camera on the James Clerk Maxwell Telescope, MNRAS, 430, 2513

Hickox, R. C., Wardlow, J. L., Smail, I., et al. 2012, The LABOCA Survey of the Extended Chandra Deep Field-South: Clustering of Submillimetre Galaxies, MNRAS, 421, 284

Hwang, H. S., & Geller, M. J. 2013, Dust-Obscured Galaxies in the Local Universe, ApJ, 769, 116

Intema, H. T., Venemans, B. P., Kurk, J. D., et al. 2006, Large-Scale Structure of Lyman Break Galaxies around a Radio Galaxy Protocluster at $z \sim 4$, A&A, 456, 433

Jones, S. F., Blain, A. W., Lonsdale, C., et al. 2015, Submillimetre Observations of WISE/Radio-Selected AGN and Their Environments, MNRAS, 448, 3325

Jones, S. F., Blain, A. W., Stern, D., et al. 2014, Submillimetre Observations of WISE-Selected High-Redshift, Luminous, Dusty Galaxies, MNRAS, 443, 146

Kim, S., Wardlow, J. L., Cooray, A., et al. 2012, *Spitzer*-IRAC Identification of *Herschel*-ATLAS SPIRE Sources, ApJ, 756, 28

Lee, J. C., Hwang, H. S., & Lee, G.-H. 2016, A Submillimeter Continuum Survey of Local Dust-Obscured Galaxies, ApJ, 833, 188

Lee, J. C., Hwang, H. S., Lee, M. G., et al. 2012, *AKARI* Near-Infrared Spectroscopy of Luminous Infrared Galaxies, ApJ, 756, 95

Magnelli, B., Popesso, P., Berta, S., et al. 2013, The Deepest Herschel-PACS Far-Infrared Survey: Number Counts and Infrared Luminosity Functions from Combined PEP/GOODS-H Observations, A&A, 553, 132

Maraston, C. 2005, Evolutionary Population Synthesis: Models, Analysis of the Ingredients and Application to High-z Galaxies, MNRAS, 362, 799

Matsuhara, H., Wada, T., Matsuura, S., et al. 2006, Deep Extragalactic Surveys around the Ecliptic Poles with *AKARI* (ASTRO-F), PASJ, 58, 673

Menéndez-Delmestre, K., Blain, A. W., Smail, I., et al. 2009, Mid-Infrared Spectroscopy of Submillimeter Galaxies: Extended Star Formation in Massive High-Redshift Galaxies, ApJ, 699, 667

Miley, G. K., Overzier, R. A., Tsvetanov, Z. I., et al. 2004, A Large Population of 'Lyman-Break' Galaxies in a Protocluster at Redshift $z \sim 4.1$, Nature, 427, 47

Miyazaki, S., Komiyama, Y., Sekiguchi, M., et al. 2002, Subaru Prime Focus Camera – Suprime-Cam, PASJ, 54, 833

Murata, K., Matsuhara, H., Wada, T., et al. 2013, *AKARI* North Ecliptic Pole Deep Survey. Revision of the Catalogue via a New Image Analysis, A&A, 559, 132

Narayanan, D., Dey, A., Hayward, C. C., et al. 2010, A Physical Model for $z \sim 2$ Dust-Obscured Galaxies, MNRAS, 407, 1701

Noble, A. G., Geach, J. E., van Engelen, A. J., et al. 2013, A Submillimetre-Bright $z \sim 3$ Overdensity Behind a $z \sim 1$ supercluster Revealed by SCUBA-2 and Herschel, MNRAS, 436, 40

Noll, S., Burgarella, D., Giovannoli, E., et al. 2009, Analysis of Galaxy Spectral Energy Distributions from Far-UV to Far-IR with CIGALE: Studying a SINGS Test Sample, A&A, 507, 1793

Oi, N., Matsuhara, H., Murata, K., et al. 2014, Optical-Near-Infrared Catalog for the *AKARI* North Ecliptic Pole Deep Field, A&A, 566, 60

Ouchi, M., Shimasaku, K., Okamura, S., et al. 2004, Subaru Deep Survey. VI. A Census of Lyman Break Galaxies at $z \sim 4$ and 5 in the Subaru Deep Fields: Clustering Properties, ApJ, 611, 685

Overzier, R. A., Miley, G. K., Bouwens, R. J., et al. 2006, Clustering of Star-Forming Galaxies Near a Radio Galaxy at $z = 5.2$, ApJ, 637, 58

Penner, K., Dickinson, M., Pope, A., et al. 2012, Evidence for a Wide Range of Ultraviolet Obscuration in $z \sim 2$ Dusty Galaxies from the GOODS-Herschel Survey, ApJ, 759, 28

Pope, A., Chary, R.-R., Alexander, D. M., et al. 2008, Mid-Infrared Spectral Diagnosis of Submillimeter Galaxies, ApJ, 675, 1171

Rigby, E. E., Hatch, N. A., Rttgering, H. J. A., et al. 2014, Searching for Large-Scale Structures around High-Redshift Radio Galaxies with Herschel, MNRAS, 437, 1882

Riguccini, L., Le Floc'h, E., Mullaney, J. R., et al. 2015, The Composite Nature of Dust-Obscured Galaxies (DOGs) at $z \sim$ 2-3 in the COSMOS Field – I. A Far-Infrared View, MNRAS, 452, 470

Seo, H., Jeong, W.-S., Kim, S. J., et al. 2017, Properties of the SCUBA-2 850 μm Sources in the XMM-LSS Field, JKAS, 50, 7

Smith, D. J. B., Dunne, L., Maddox, S. J., et al. 2011, *Herschel*-ATLAS: counterparts from the Ultraviolet-Near-Infrared in the Science Demonstration Phase Catalogue, MNRAS, 416, 857

Sutherland, W., & Saunders, W. 1992, On the Likelihood Ratio for Source Identification, MNRAS, 259, 413

Takata, T., Sekiguchi, K., Smail, I., et al. 2006, Rest-Frame Optical Spectroscopic Classifications for Submillimeter Galaxies, ApJ, 651, 713

Toba, Y., Nagao, T., Kajisawa, M., et al. 2017a, Clustering of Infrared-Bright Dust-Obscured Galaxies Revealed by the Hyper Suprime-Cam and WISE, ApJ, 835, 36

Toba, Y., Nagao, T., Wang, W.-H., et al. 2017b, Far-Infrared Properties of Infrared-Bright Dust-Obscured Galaxies Selected with IRAS and *AKARI* Far-Infrared All-Sky Survey, ApJ, 840, 21

Venemans, B. P., Kurk, J. D., Miley, G. K., et al. 2002, The Most Distant Structure of Galaxies Known: A Protocluster at $z = 4.1$, ApJ, 569, L11

Venemans, B. P., Röttgering, H. J. A., Miley, G. K., et al. 2007, Protoclusters Associated with $z > 2$ Radio Galaxies. I. Characteristics of High Redshift Protoclusters, A&A, 461, 823

Wang, L., Viero, M., Clarke, C., et al. 2014, HerMES: Point Source Catalogues from Herschel-SPIRE Observations II, MNRAS, 444, 2870

Wardlow, J. L., Smail, Ian, Coppin, K. E. K., et al. 2011, The LABOCA Survey of the Extended Chandra Deep Field-South: A Photometric Redshift Survey of Submillimetre Galaxies, MNRAS, 415, 1479

Wilkinson, A., Almaini, O., Chen, C.-C., et al. 2017, The SCUBA-2 Cosmology Legacy Survey: the Clustering of Submillimetre Galaxies in the UKIDSS UDS Field, MNRAS, 464, 1380

Wuyts, S., Förster, S,, Natascha, M., Lutz, D., et al. 2011, On Star Formation Rates and Star Formation Histories of Galaxies Out to $z \sim 3$, ApJ, 738, 106